Optics Letters

Rapid functional optoacoustic micro-angiography in a burst mode

Urs A. T. Hofmann,[1,2] Johannes Rebling,[1,2] Héctor Estrada,[1,2] Pavel Subochev,[3] and Daniel Razansky[1,2,*]

[1]Institute of Pharmacology and Toxicology and Faculty of Medicine, University Zurich, Winterthurerstrasse 190, 8057 Zurich, Switzerland
[2]Institute for Biomedical Engineering and Department of Information Technology and Electrical Engineering, ETH Zurich, Wolfgang-Pauli-Str. 27, 8093 Zurich, Switzerland
[3]Institute of Applied Physics RAS, 46 Ulyanov Street, Nizhny Novgorod 603950, Russia
*Corresponding author: daniel.razansky@uzh.ch

Received 10 January 2020; revised 16 February 2020; accepted 28 February 2020; posted 2 March 2020 (Doc. ID 387630); published 0 MONTH 0000

Optoacoustic microscopy (OAM) can image intrinsic optical absorption contrast at depths of several millimeters where state-of-the-art optical microscopy techniques fail due to intense light scattering in living tissues. Yet, wide adoption of OAM in biology and medicine is hindered by slow image acquisition speed, small field of view (FOV), and/or lack of spectral differentiation capacity of common system implementations. We report on a rapid acquisition functional optoacoustic micro-angiography approach that employs a burst-mode laser triggering scheme to simultaneously acquire multi-wavelength 3D images over an extended FOV covering 50 mm × 50 mm in a single mechanical overfly scan, attaining 28 and 14 μm resolution in lateral and axial dimensions, respectively. Owing to an ultrawideband low-noise design featuring a spherically focused polyvinylidene difluoride transducer, we demonstrate imaging of human skin and underlying vasculature at up to 3.8 mm depth when using per-pulse laser energies of only 25 μJ without employing signal averaging. Overall, the developed system greatly enhances the performance and usability of OAM for dermatologic and micro-angiographic studies.

https://doi.org/10.1364/OL.387630

Human skin is a difficult target for noninvasive investigations, owing primarily to its optically heterogeneous and highly scattering nature. Optical dermoscopy is a standard tool in dermatology for inspecting skin lesions via classification and categorization of microscopic surface features inaccessible by the naked eye [1]. In human skin, strong light scattering from the rough and curved stratum corneum and underlying layers limits the effective imaging depth of optical microscopy methods to just a few hundred micrometers [2], making lesions such as melanoma with average Breslow thickness of 0.72 mm only partially accessible by optical imaging techniques [3]. High-definition optical coherence tomography (OCT) has also been shown to discriminate between skin malignancies, yet its clinical application is similarly limited to imaging of superficial skin layers, further suffering from lack of functional and molecular contrast [4]. Overall, the lack of appropriate *in vivo* imaging methodologies leads to extensive use of biopsies in dermatology [3].

Optoacoustic (OA) imaging has recently evolved as a promising approach attaining rich optical absorption contrast and high spatial resolution in deep tissues by detecting laser-generated broadband ultrasound (US) waves [5]. Several OA microscopy (OAM) and mesoscopy systems have been studied as a viable noninvasive alternative to histopathological analysis of biopsied skin [6–10]. Clinical progress is hindered mainly by the limited technical performance of existing implementations. While long scanning times typically result in motion artifacts and diminished image quality [11,12], the limited field of view (FOV) of most systems hinders their effective use for imaging human skin lesions, such as melanoma with an average size of (12.8 ± 7.8) mm [13]. Other constraints stem from the shallow penetration depth of 1 mm [6,7], inadequate for imaging across all the human skin layers extending up to 5 mm depth. Furthermore, most existing systems operate at a single or narrow wavelength range while chiefly focusing on imaging vascular anatomy. On the other hand, multi-wavelength solutions often require successive mechanical scanning at each wavelength, resulting in long data acquisition times and severe motion artifacts, further inhibiting *in vivo* applicability [11].

We developed a rapid acquisition functional OA micro-angiography (FOMA) approach to overcome limitations of existing OAM systems. In particular, using a burst-mode trigger scheme, large skin areas of up to 50 mm × 50 mm can be imaged at several optical wavelengths within a single overfly scan.

A schematic representation of the imaging system is shown in Fig. 1. Three nanosecond pulsed laser sources running at up to 100 kHz pulse repetition frequency (PRF) are employed

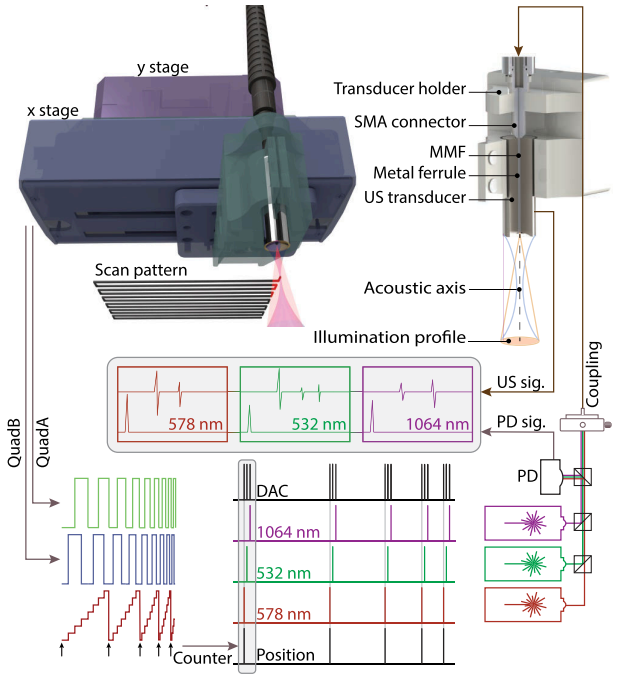

Fig. 1. Schematic diagram of the system for rapid functional optoacoustic micro-angiography (FOMA) in a burst mode. FOV covering 50 mm × 50 mm area is scanned in a zig-zag pattern using a continuous overfly scan. Three laser sources at 532, 578, and 1064 nm are combined and coupled into a multimode fiber (MMF) after redirecting 1% of the beam into a photodiode [PD]. The position of the fast-moving stage is monitored with 200 nm accuracy by reading out its quadrature encoder signal [QuadA/QuadB]. Following each predefined incremental stage movement, all three lasers are triggered in a cascade with a short 6 µs delay with the stage in constant motion. By averting acceleration and deceleration at each scan position, we enable rapid acquisition of multi-wavelength data free of motion artifacts.

to illuminate the sample. Two of the sources have fixed wavelengths of 532 and 1064 nm (Onda 532 nm and 1064 nm, Bright Solutions, UK) while the third source is a tunable dye laser (Credo, Sirah Lasertechnik, Germany) whose wavelength was set to 578 nm as a non-isosbestic point of hemoglobin in the current study. The per-pulse energy (PPE) of each beam is adjustable through a half-wave plate followed by a polarizing beam splitter. Two dichroic mirrors (DMLP550 and DMSP805, Thorlabs, USA) combine the three beams into a single optical axis. A beam sampler (BSF10-A, Thorlabs, USA) redirects approximately 1% of the combined beam into a photodiode (PD) to monitor PPEs and delays of the individual light pulses (DET10A2, Thorlabs, USA). Light is coupled into a MMF (0.22 NA, 200 µm core diameter, FG200LCC, Thorlabs, USA) using a 100 mm focusing lens (AC254-100-A-ML, Thorlabs, USA) and a two-dimensional adjustable stage (CXY1, Thorlabs, USA).

A custom-made, 9 µm foil polyvinylidene difluoride (PVDF) spherically focused transducer (7 mm focal distance and 0.43 NA) detects the optoacoustically generated waves (Figs. 2(A) and 2(B)) using a custom-made 34 dB impedance-matching amplifier with 1 to 100 MHz bandwidth (−6). The MMF is guided through a central hole in the transducer allowing concentric alignment of the light cone and acoustic axis [14]. The detected OA signals are amplified in the transducer housing followed by additional off-site amplification positioned in a Faraday cage (24 dB, ZFL-500LN, Mini-Circuits, USA). A dual-channel, 16 bit resolution data acquisition card (DAC) (M4I.4420-X8, Spectrum Systementwicklung Microelectronic, Germany) simultaneously digitizes transducer and PD signals at 250 MSps for each transducer position and wavelength. The transducer is held by two perpendicularly arranged stages. During imaging, a fast-moving stage (DDSM50-M, Thorlabs, UK) continuously oscillates between the edges of the imaged area with 0.5 m/s maximum velocity and 3.5 m/s^2 acceleration, while the second stage (M683, Physik Instrumente, Germany) moves incrementally following each B-scan, thus resulting in a zig-zag scan pattern. A microcontroller (Teensy 3.6, PJRC, USA) reads the quadrature encoder signal of the fast-moving stage, detecting incremental stage movements down to 200 nm. An internal counter tracks relative stage position and generates a trigger signal depending on the step size defined prior to scanning through a serial-based MATLAB interface. A second microcontroller (Teensy 4.0, PJCR, USA) translates the position trigger into a burst-mode cascade by shooting all three lasers shortly after each other with 6 µs temporal delay sufficient to avoid crosstalk between OA data recorded at each excitation wavelength. Laser and data acquisition are triggered for each wavelength and stage position, resulting in minimal memory consumption, a regularly spaced volume grid, and no laser pulse overshoot near the edges of the imaged area where the fast stage is accelerating or decelerating.

The recorded OA responses are bandpass filtered between 0.5 and 120 MHz using a first-order Butterworth filter. PPE is calculated by integrating the PD signal after subtracting the noise level. The precise instants of the laser shots are further extracted by identifying maxima in the PD curves. The recorded OA waveforms are then individually corrected for laser delays and energy fluctuations. A synthetic aperture focusing technique (SAFT) was applied to the preprocessed data where each reconstructed point is rated by the wavefront coherence to reduce smearing in lateral dimension [16–19]. After reconstruction, the volume is deconvolved with a point spread function extracted from reconstructed microsphere measurements to further improve lateral resolution and signal-to-noise ratio (SNR) [20]. The reconstruction procedure is visualized for a microsphere in Fig. 2(E). By employing a graphics processing unit (GPU) (CUDA 10.0, RTX2070S, NVIDIA, USA), datasets containing 2×10^9 voxels over 20 mm × 20 mm × 5 mm are reconstructed within 10 min. Phantom measurements using 10 to 20 µm diameter microspheres (BKPMS-1.2, Cospheric, USA) sparsely distributed in 0.5% agar allowed for an automatic determination of the exact transducer's focal distance (6.85 mm) and speed of sound in both agar and water (1484 m/s). Experiments were performed at 50 mm/s peak velocity of the stage and 5 µm step size, resulting in PRFs of up to 10 kHz. The measurements further revealed an ultrawideband sensitivity of the PVDF transducer exceeding 100 MHz (Figs. 2(A) and 2(B)), which was determined by also taking into account frequency-dependent absorption of US waves in deionized water. The effective lateral and axial spatial resolutions of the system were measured to be (28 ± 8) µm and (14 ± 2) µm, respectively (see Fig. 2(C)). Variability of the lateral resolution can be attributed to fluctuations of the microsphere diameter (10 to 20 µm). Figure 2(D) further shows an example of raw OA

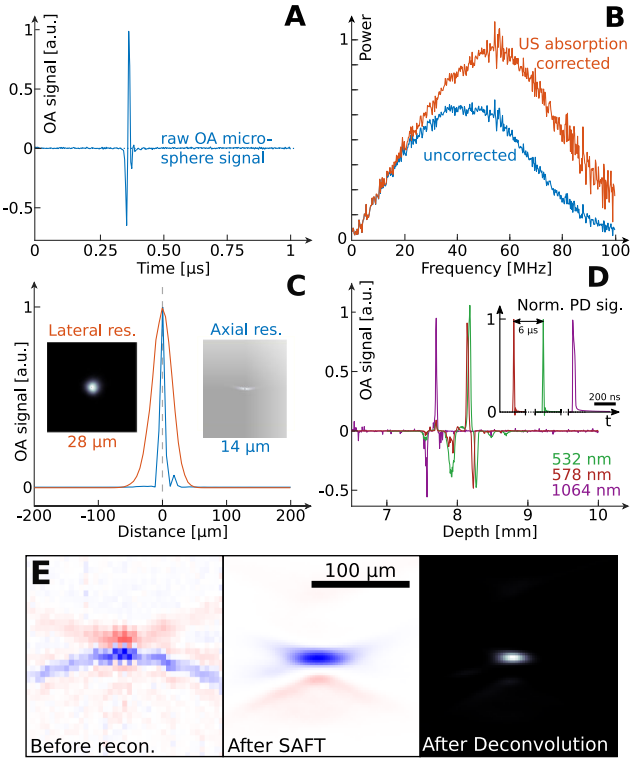

Fig. 2. Characterization of imaging performance. (A) Raw OA signal emitted by a 10 μm sphere embedded in agar. (B) Microsphere signal spectrum before (blue) and after (red) correcting for frequency-dependent US attenuation in water [15], exhibiting a useful detection bandwidth beyond 100 MHz. (C) Reconstructed cross-sectional OA slices through microsphere revealing full width half maximum (FWHM) of (28 ± 8) μm and (14 ± 2) μm in lateral and axial directions, respectively. (D) Example of raw OA waveforms detected from human skin at the three wavelengths and corresponding PD signals. (E) Reconstruction procedure applied to a microsphere below transducer focus showing cross sections before SAFT, after SAFT, and after applying deconvolution.

waveforms detected from human skin at the three wavelengths and the corresponding PD signals.

Skin of a healthy volunteer was then imaged using the developed system. Step size was set to 25 μm while limiting velocity of the fast-moving stage to 100 mm/s, which resulted in a maximum PRF of 4 kHz. PPE was set to 25 μJ at 532 and 578 nm (corresponding to 0.46 mJ/cm^2 to 1.07 mJ/cm^2 fluence at the skin surface) and 100 μJ at 1064 nm (corresponding to 1.84 mJ/cm^2 to 4.30 mJ/cm^2 fluence at the skin surface), being within the safety limit for individual laser pulses (ANSI Z136.1-2014). Furthermore, a MATLAB script (see Code 1, [21]) calculated the exposure of multiple laser pulses for the given scan pattern taking stage acceleration and velocity profiles as well as time range and wavelength-dependent safety limits into account. The safety limits were also observed for the average laser intensity on the skin surface for all the used wavelengths.

Vasculature over full skin thickness was revealed reaching up to 3.8 mm depth (see Visualization 1 Animation 1, [22]). Note that no averaging was used for phantom or skin imaging. Due to broadband sensitivity of PVDF, vascular networks containing vessels with diameters ranging from 10 μm up to 2 mm can be imaged (Fig. 3(A)). By bandpass filtering the detected OA signals at low (5 to 25 MHz) and high (30 to 120 MHz) frequencies, differently sized vessels can be readily differentiated in the side-view projection. Although the lateral resolution is not sufficient to resolve capillaries inside a 28 μm spot, our highly sensitive system can still detect their OA footprint. When inspecting the multi-wavelength data, the images manifested several vascularized skin layers known as subpapillary, cutaneous, and deep plexus (Fig. 3(C)). Capillary loops and plexus can be distinguished based on vessel orientation, z position extracted from 3D datasets, vessel size extracted from frequency content (Fig. 3(B)), and comparison to previously performed studies [6]. Since no vessels pass through the dermal–epidermal junction, the epidermal layer is avascular formed by 95% of kreatinocytes mixed with melanocytes, Langerhans' cells, and Merkel cells [23]. Since melanin has a broad optical absorption spectrum, the OA signal at the 1064 nm excitation wavelength in the infrared (IR) is concentrated mainly in the outermost epidermal layer. Arterioles are surrounded by elastic tissue that contains smooth muscle cells, elastin, and collagen fibers [23], thus further providing signal in the IR. The 1064 nm wavelength is also absorbed in the uppermost layer of the epidermis (stratum corneum) revealing fibrous-like orientation along the skin surface.

While our current FOMA implementation can image very large FOV of 20 mm × 20 mm at multiple wavelengths within an unprecedentedly short duration of 2 min (see Visualization 1 Table 1), the imaging speed could be further improved by combining two mechanical stages with a microelectromechanical system (MEMS) scanner oscillating over shorter distances, at the trade-off of smaller FOV and increased complexity, cost, and weight. Furthermore, mounting of stages, transducer, and fiber on a passive robotic arm may extend usability to less accessible regions of the human body [6]. The use of laser diodes would allow more compact optics and therefore bedside imaging in clinical settings, potentially also reducing the overall cost. Nevertheless, intense pulses with ultrashort durations in the few nanosecond range are difficult to achieve with laser diode technology, resulting in reduced spatial resolution or otherwise insufficient PPE and low SNR and penetration depth [24]. In terms of image reconstruction, model-based inversion schemes allow for a more accurate representation of the measurement geometry, and thus could aid in mitigating limited-view artifacts and achieving better image quantification performance [25]. Unmixing for deoxygenated and oxygenated blood could be performed based on 532 and 578 nm absorption after incorporating accurate fluence models.

In conclusion, we developed a functional FOMA system incorporating a burst-mode trigger scheme that allows multispectral image acquisition in a single rapid mechanical overfly scan without employing signal averaging, thus averting motion between the consecutive wavelengths. The system's performance is showcased by imaging vasculature over the full human skin depth. Large volumes over a 50 mm × 50 mm area are scanned at resolutions down to the capillary level within several minutes. The laser triggering speed is adjusted according to the precise positions read from the stage quadrature encoder, which allows to render a uniform image grid and avoid pulse overshoot and excessive laser exposure at the stage turning points. The system allows imaging at a broad spectral window spanning from 532 to 1064 nm, which can be used for distinguishing different anatomical structures or performing functional imaging of,

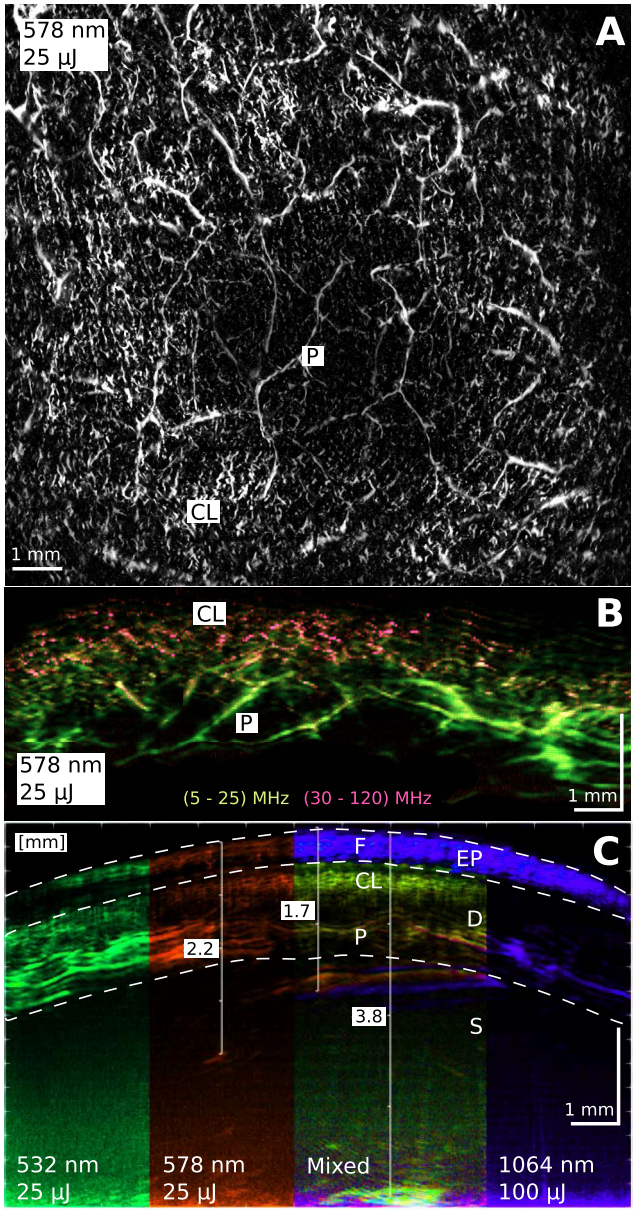

Fig. 3. Large-area microvascular network in a human palm acquired at three wavelengths within 2 min. (A) Maximum intensity projection of the 3D FOAM image at 578 nm showing vasculature of the plexus [P] and capillary loops in the upper dermal layer [CL]. (B) Single wavelength image at 578 nm bandpass filtered in different acoustic frequency bands to distinguish small capillary loops in superficial layers from larger vessels in the plexus. (C) Complication of cross-sectional images at three wavelengths: melanin is present in the epidermis [EP], while vasculature is limited to the dermis [D] and subcutaneous tissue [S]. Fibrous structures [F] are visible within the epidermis. Note that vasculature was resolved down to 3.8 mm depth in a highly scattering and absorbing tissue.

e.g., oxygen saturation. Note that the 1064 nm wavelength is less absorbed by the skin as compared to visible light. Besides deeper penetration into biological tissue, this wavelength range is recently becoming attractive due to development of new contrast agents tailored for the second near-IR window [26]. All in all, the developed system overcomes several drawbacks of the existing implementations and represents an important step towards wider adoption of OA microscopy and mesoscopy for biomedical and clinical applications.

Funding. Russian Science Foundation (18-45-06006); Helmholtz Association (HRSF-0020).

Disclosures. The authors declare no conflicts of interest.

REFERENCES

1. G. Argenziano and H. P. Soyer, Lancet Oncol. **2**, 443 (2001).
2. R. R. Anderson, B. S. Parrish, and J. A. Parrish, J. Invest. Dermatol. **77**, 13 (1981).
3. H. M. Rolfe, Australas. J. Dermatol. **53**, 112 (2012).
4. M. A. L. M. Boone, M. S. F. Dhaenens, M. Miyamoto, A. Marneffe, G. B. E. Jemec, V. D. Marmol, and R. Nebosis, Arch. Dermatol. Res. **308**, 7 (2016).
5. X. L. Deán-Ben, S. Gottschalk, B. M. Larney, S. Shohamc, and D. Razansky, Chem. Soc. Rev. **46**, 2158 (2017).
6. J. Aguirre, M. Schwarz, N. Garzorz, M. Omar, A. Buehler, K. Eyerich, and V. Ntziachristos, Nat. Biomed. Eng. **1**, 0068 (2017).
7. J.-T. Oh, M.-L. Li, H. F. Zhang, K. Maslov, G. Stoica, and L. V. Wang, J. Biomed. Opt. **11**, 34032 (2006).
8. M. Omar, J. Aguirre, and V. Ntziachristos, Nat. Biomed. Eng. **3**, 354 (2019).
9. E. Z. Zhang, J. G. Laufer, R. B. Pedley, and P. C. Beard, Phys. Med. Bio. **54**, 1035 (2009).
10. E. Z. Zhang, B. Povazay, J. Laufer, A. Alex, B. Hofer, B. Pedley, C. Glittenberg, B. Treeby, B. Cox, P. Beard, and W. Drexler, Biomed. Opt. Express **2**, 2202 (2011).
11. M. Schwarz, N. Garzorz-Stark, K. Eyerich, J. Aguirre, and V. Ntziachristos, Sci. Rep. **7**, 10386 (2017).
12. H. Zhao, N. Chen, T. Li, J. Zhang, R. Lin, X. Gong, L. Song, Z. Liu, and C. Liu, IEEE Trans. Med. Imaging **38**, 2139 (2019).
13. A. Pinero-Madrona, J. Am. Acad. Dermatol. **80**, 806 (2019).
14. H. Estrada, J. Turner, M. Kneipp, and D. Razansky, Laser Phys. Lett. **11**, 045601 (2014).
15. J. Krautkrämer, *Ultrasonic Testing of Materials*, 4th ed. (Springer-Verlag, 1990).
16. J. Turner, H. Estrada, M. Kneipp, and D. Razansky, Optica **4**, 770 (2017).
17. M.-L. Li, H. F. Zhang, K. Maslov, G. Stoica, and L. V. Wang, Opt. Lett. **31**, 474 (2006).
18. C.-K. Liao, M.-L. Li, and P.-C. Li, Opt. Lett. **29**, 2506 (2004).
19. V. V. Perekatova, M. Y. Kirillin, I. V. Turchin, and P. V. Subochev, J. Biomed. Opt. **23**, 1 (2018).
20. D. Cai, Z. Li, Y. Li, Z. Guo, and S.-L. Chen, Opt. Express **25**, 1421 (2017).
21. U. A. T. Hofmann, "Laser exposure limit calculation for rasterscan optoacoustic microscopy," 2020, https://doi.org/10.6084/m9.figshare.11859771.v1.
22. U. A. T. Hofmann, "Multiwavelength acoustic resolution opto-acoustic microscopy of human palm," 2020, https://doi.org/m9.figshare.11859816.v1.
23. J. A. McGrath, R. A. J. Eady, and F. M. Pope, *Anatomy and Organization of Human Skin* (Wiley, 2004), Chap. 3, pp. 45–128.
24. X. Dai, H. Yang, and H. Jiang, Opt. Lett. **42**, 1456 (2017).
25. X. L. Deán-Ben, H. Estrada, M. Kneipp, J. Turner, and D. Razansky, Proc. SPIE **8943**, 89434V (2014).
26. K. Homan, S. Kim, Y.-S. Chen, B. Wang, S. Mallidi, and S. Emelianov, Opt. Lett. **35**, 2663 (2010).

Queries

1. AU: Please check and confirm the insertion of the acronym "OAM" on first occurrence of its expansion in the body text.

2. AU: Please expand the acronym "MMF" on first occurrence.

3. AU: The funding information for this article has been generated using the information you provided to OSA at the time of article submission. Please check it carefully. If any information needs to be corrected or added, please provide the full name of the funding organization/institution as provided in the CrossRef Open Funder Registry (https://search.crossref.org/funding).